

# Heterogeneously Integrated Graphene/Silicon/Halide Waveguide Photodetectors toward Chip-Scale Zero-Bias Long-Wave Infrared Spectroscopic Sensing

Yiming Ma, Yuhua Chang, Bowei Dong, Jingxuan Wei, Weixin Liu, and Chengkuo Lee\*



Cite This: *ACS Nano* 2021, 15, 10084–10094



Read Online

ACCESS |



Metrics & More



Article Recommendations



Supporting Information

**ABSTRACT:** Mid-infrared absorption spectroscopy plays an important role in molecule identification and quantification for widespread applications. Integrated photonics provides opportunities to perform spectroscopic sensing on-chip for the minimization of device size, cost, and power consumption. The integration of waveguides and photodetectors is an indispensable step toward the realization of these on-chip sensing systems. It is desired to extend the operating wavelengths of these on-chip sensing systems to the long-wave infrared (LWIR) range to utilize more molecular absorption fingerprints. However, the development of LWIR waveguide-integrated photodetectors faces challenges from both waveguide platforms due to the bottom cladding material absorption and photodetection technologies due to the low LWIR photon energy. Here, we demonstrate LWIR waveguide-integrated photodetectors through heterogeneous integration of graphene photodetectors and Si waveguides on CaF<sub>2</sub> substrates. A high-yield transfer printing method is developed for flexibly integrating the waveguide and substrate materials to solve the bottom cladding material absorption issue. The fabricated Si-on-CaF<sub>2</sub> waveguides show low losses in the broad LWIR wavelength range of 6.3–7.1 μm. The graphene photodetector achieves a broadband responsivity of ~8 mA/W in these low-photon-energy LWIR wavelengths under zero-bias operation with the help of waveguide integration and plasmonic enhancement. We further integrate the graphene photodetector with a Si-on-CaF<sub>2</sub> folded waveguide and demonstrate on-chip absorption sensing using toluene as an example. These results reveal the potential of our technology for the realization of chip-scale, low-cost, and low-power-consumption LWIR spectroscopic sensing systems.

**KEYWORDS:** long-wave infrared, photodetector, graphene, silicon photonics, integrated photonics, absorption spectroscopy

Mid-infrared (MIR, 2–20 μm) absorption spectroscopy provides a powerful tool for label-free discrimination and quantification of molecules through their characteristic vibrational transitions, with applications ranging from industrial process control to medical diagnostics and from environmental monitoring to trace gas detection on Mars by NASA's Curiosity Mars Rover.<sup>1–5</sup> Conventional spectrometers rely on free-space optics that are bulky, expensive, and power-hungry, while integrated photonics promises the ability to perform the same analysis using chips with high compactness, low cost, and low power consumption.<sup>6,7</sup> The integration of waveguides and photodetectors is a critical step toward the realization of these chip-scale sensing systems. Despite the advances made in the short- and mid-wave infrared (SWIR, 2–3 μm; MWIR, 3–6 μm) integrated photonics, it is desired to extend the working wavelengths to the long-wave infrared (LWIR) range beyond 6

μm to make more use of molecular absorption fingerprints.<sup>8–10</sup> However, the development of LWIR waveguide-integrated photodetectors faces challenges from both waveguide platforms and photodetection technologies, as illustrated in Figure 1a.

The common silicon-on-insulator (SOI) and silicon nitride-on-insulator (SNOI) waveguide platforms,<sup>11,12</sup> as well as germanium-on-insulator (GOI),<sup>13</sup> can operate only up to ~4 μm limited by the strong absorption from the buried oxide

Received: March 3, 2021

Accepted: May 26, 2021

Published: June 1, 2021



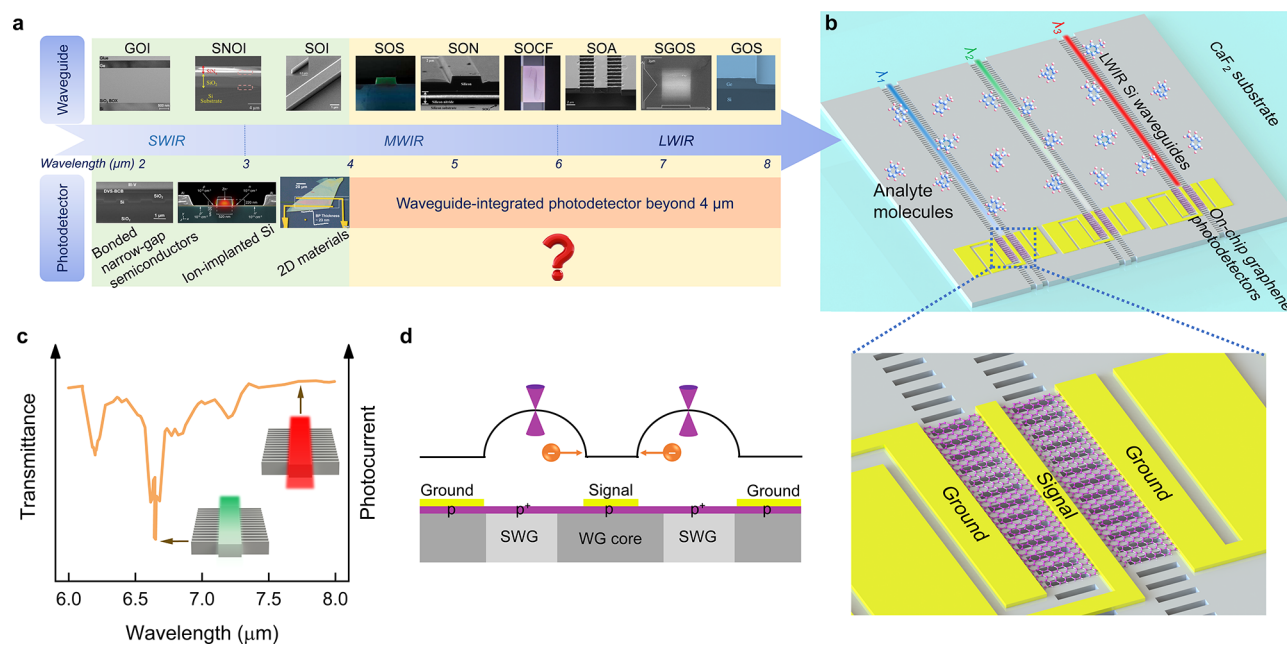


**Figure 1. Design concept.** (a) Development roadmap of MIR waveguides and waveguide-integrated photodetectors. Waveguide-integrated photodetector operating beyond  $4\ \mu\text{m}$  has not been demonstrated yet, to the best of our knowledge. Reprinted with permission from refs 11–15, 18, 22, 25, 26, 33. Copyright 2017 IEEE, 2013 Wiley-VCH, 2016 The Optical Society, 2010 The Optical Society, 2013 AIP Publishing, 2014 The Optical Society, 2014 American Chemical Society, 2016 The Optical Society, 2014 The Optical Society, and 2019 American Chemical Society, respectively. Reprinted with permission under a Creative Commons Attribution 4.0 License from refs 16 and 17. Copyright 2018 The Optical Society and 2017 The Optical Society, respectively. (b) Artist's impression of the envisioned on-chip LWIR spectroscopic sensor featuring transfer-printed SOCF multichannel waveguides integrated with graphene photodetectors and zoom-in view of the waveguide-integrated graphene photodetector with GSG electrode configuration. (c) Sketch of the on-chip sensing mechanism using toluene as an example. At toluene's absorption peak ( $6.65\ \mu\text{m}$ ), the light transmission intensity in the waveguide is significantly attenuated, leading to weaker photoresponse of the graphene photodetector. (d) Band diagram of the graphene photodetector at zero bias. The inhomogeneous doping levels enable photocarrier collection.

(BOX) layer. Similarly, the bandwidths of silicon-on-sapphire (SOS) and silicon-on-nitride (SON) platforms are limited to  $\sim 5.5\ \mu\text{m}$  by their bottom cladding materials.<sup>14,15</sup> To achieve working wavelength extension, several LWIR platforms have been reported recently, such as suspended silicon-on-air (SOA),<sup>16</sup> germanium-on-silicon (GOS),<sup>17</sup> and silicon–germanium alloy-on-silicon (SGOS),<sup>18</sup> with low propagation losses of a few dB/cm. Nevertheless, the suspended waveguides pose difficulties in following processes and further integration. Although GOS and SGOS waveguides have shown promising performance for LWIR applications, it is still worth fully leveraging the most mature, cheap, and easily accessible SOI platform and Si transparency window up to  $8\ \mu\text{m}$ . Motivated by this, a transfer printing technique proves its feasibility to transfer the Si device layer from SOI onto new substrates without the involvement of any adhesive that may compromise the optical properties of Si. This transfer printing technique has been reported mostly for the fabrication of microelectronic and optoelectronic devices on flexible substrates<sup>19–21</sup> but rarely for the heterogeneous integration of photonic devices. Chen *et al.* transfer-printed Si photonic devices onto a calcium fluoride ( $\text{CaF}_2$ ) substrate,<sup>22</sup> which is a type of halide transparent up to  $8\ \mu\text{m}$  and with a low refractive index of  $\sim 1.4$ . Although the demonstrated ring-resonator-based spectroscopy around  $5.2\ \mu\text{m}$  is interesting, their transfer scheme is complicated and demands a very precise control on the size of photoresist pedestals, leading to difficulties in retrieving an intact membrane from SOI. A simplified method with a higher yield is desired.

State-of-the-art MIR photodetectors are typically based on narrow-band-gap semiconductors such as HgCdTe (MCT) and III–V alloys. Because of their huge lattice mismatch with Si, their integration with waveguides relies on adhesive bonding processes.<sup>23–25</sup> A monolithic photodetector integration approach builds on ion-implanted Si.<sup>26–28</sup> The main disadvantage of this kind of photodetectors is their low responsivities due to the weak extrinsic dopant or defect-level-mediated absorption. Emerging two-dimensional (2D) materials are regarded as a promising alternative solution for on-chip photodetection, whose direct monolithic integration with Si is enabled by their layered lattice structures. Various 2D materials with different band gaps can realize a very wide response range across the electromagnetic spectrum.<sup>29</sup> Hexagonal boron nitride with a large band gap of  $\sim 6\ \text{eV}$  enables solar-blind deep ultraviolet photodetectors.<sup>30</sup> Numerous transition metal dichalcogenides with band gaps typically ranging from 1 to 2 eV cover visible and near-infrared (NIR) wavelengths.<sup>31</sup> Black phosphorus (BP) possesses a narrow band gap of  $\sim 0.33\ \text{eV}$  in its bulk form, pushing the cutoff wavelength to  $4.13\ \mu\text{m}$ .<sup>32</sup> Recently, MWIR waveguide-integrated BP photodetectors operating from  $3.68$  to  $4.03\ \mu\text{m}$  were reported.<sup>33</sup> For photodetection at longer wavelengths, semimetallic materials such as graphene become suitable choices.<sup>34</sup> Their gapless nature endows them with high-speed broadband photoresponse from ultraviolet to terahertz while also resulting in a large dark current when bias is applied, reducing the detection sensitivity.<sup>35–37</sup> Zero-bias operation is thus preferred to reduce the dark current as well as the power consumption.

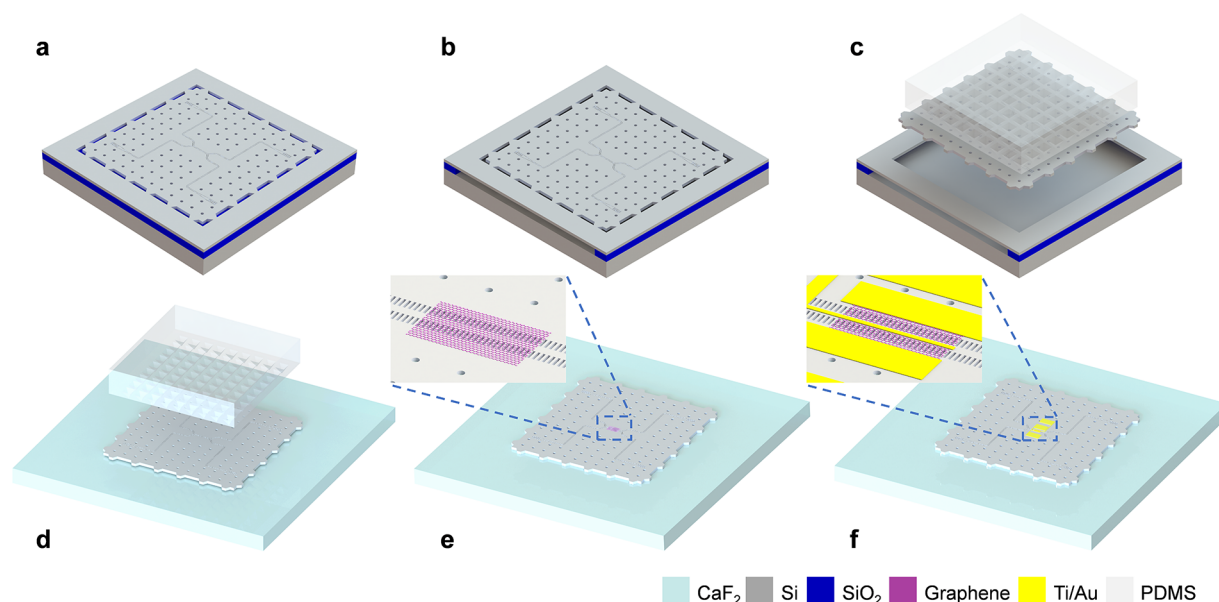


**Figure 2.** Fabrication process for waveguide transfer printing and on-chip photodetector integration. (a) Membrane patterning by lithography and dry etching. (b) DHF release of BOX layer. (c) Membrane retrieval by PDMS stamp. (d) Membrane printing onto  $\text{CaF}_2$  substrate. (e) Graphene transfer onto waveguide. (f) Electrode patterning by lift-off.

Under zero-bias operation, the photocarrier separation is achieved less efficiently *via* photovoltaic (PV) and photo-thermoelectric (PTE) effects, which compromises the responsivity.<sup>38–40</sup> To improve the responsivity, a strategy based on hybrid integration of graphene photodetectors with waveguides and plasmonic structures was demonstrated in the NIR.<sup>41–44</sup> The waveguides extend the light–matter interaction length from the absorption material thickness to the longitudinal dimension of the material, while the plasmonic structures concentrate the optical field in their vicinity to enhance the light–matter interaction. Nevertheless, due to the lower absorption of graphene in the LWIR,<sup>45</sup> it is unclear whether a high responsivity comparable to that of NIR counterparts can be achieved in graphene LWIR photodetectors through this improvement strategy.

In this work, we present LWIR waveguide-integrated zero-bias photodetectors based on heterogeneous integration of graphene photodetectors and Si waveguides on  $\text{CaF}_2$  substrates. To address the waveguide platform issue, a simple transfer printing method utilizing a microstructured polydimethylsiloxane (PDMS) stamp is developed to facilitate the transfer of large-scale membranes containing waveguides from the SOI device layer onto  $\text{CaF}_2$  substrates with high yield. The transfer-printed Si-on- $\text{CaF}_2$  (SOCF) waveguides show low propagation loss, bending loss, and Y-junction insertion loss in the broad wavelength range of 6.3–7.1  $\mu\text{m}$ . The photodetection technology issue is addressed by employing waveguide-integrated graphene photodetectors with a ground–signal–ground (GSG) electrode configuration. The signal electrode on top of the waveguide not only enables zero-bias photodetection but also provides plasmonic enhancement. The achieved broadband responsivity of around 8 mA/W is comparable with that of NIR counterparts. The waveguide-integrated graphene photodetector is further utilized for on-chip absorption sensing using toluene vapor as an example. A limit of detection (LoD) of 0.48% is experimentally assessed. Our proposed technology shows promising potential for the

realization of chip-scale LWIR spectroscopic sensing systems with low cost and low power consumption.

## RESULTS AND DISCUSSION

**Design Concept.** Figure 1b schematically illustrates our envisioned on-chip LWIR spectroscopic sensor based on our proposed technology, which features transfer-printed SOCF multichannel waveguides integrated with graphene photodetectors employing the GSG electrode configuration. With the light at different wavelengths propagating in the multiple waveguide channels, the surrounding analyte molecules extensively interact with the evanescent field. As a result, the light transmission intensity, and thus the graphene photo-response, is significantly weakened at the molecular absorption peaks compared with other wavelengths, as depicted in Figure 1c. Figure 1d portrays the zero-bias operation mechanism of the graphene photodetector. Because of different doping levels in the metal-covered (p-doped) and uncovered (p<sup>+</sup>-doped because of adsorbates from the ambient air) parts of graphene, junctions with built-in gradients of electrostatic potential and Seebeck coefficient are formed near both sides of the middle signal electrode. These metal-doped graphene junctions not only exist at the metal/graphene interfaces but also extend tens of nanometers into the graphene channels, enabling effective separation and collection of photogenerated electron–hole pairs.<sup>40,46</sup>

**Integration Method.** Figure 2 presents the fabrication process for the heterogeneously integrated photonic system. A 2.4 mm  $\times$  2.4 mm membrane is first patterned on the 1.5  $\mu\text{m}$  thick Si device layer. This membrane, which is supported by periodic trapezoidal beams, contains grating couplers, transverse-electric (TE) waveguides with subwavelength grating (SWG) claddings, and releasing holes. The SWGs provide mechanical support for waveguides in the following BOX wet etching and retrieval steps. The releasing holes are arrayed with 2  $\mu\text{m}$  radius and 25  $\mu\text{m}$  period for a trade-off between membrane stiffness and wet etching time. After the membrane is fully etched, the 3  $\mu\text{m}$  thick BOX layer beneath the

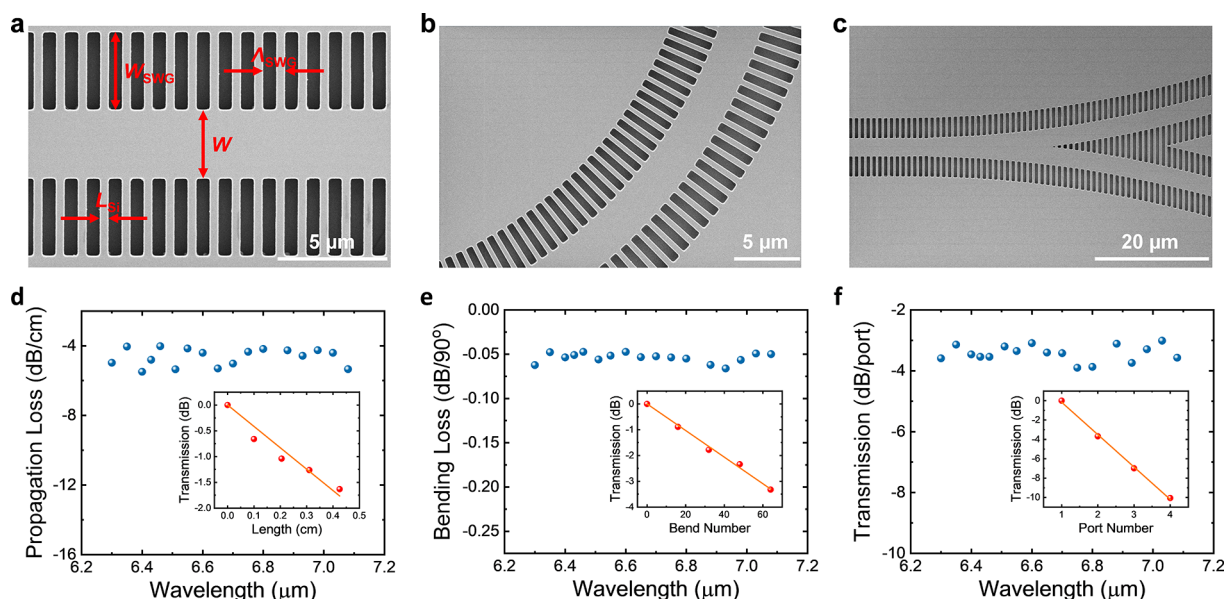


**Figure 3.** Loss characterization of transfer-printed SOCF waveguides. SEM images of (a) waveguide with SWG cladding, (b) 90° bend, and (c) Y-junction. Broadband spectra of (d) propagation loss, (e) bending loss, and (f) Y-junction transmission in 6.3–7.1  $\mu\text{m}$ . The insets show representative cut-back measurement results at 6.55  $\mu\text{m}$ .

membrane is locally removed in diluted hydrofluoric acid (DHF) solution, followed by drying in a critical point dryer (CPD) to avoid membrane's stiction to the Si handle layer.

To transfer print the membrane, a reversible surface adhesion is critical, which is enabled by a PDMS stamp with microstructured pyramids (see Figure S1 for the PDMS stamp fabrication process). These pyramids are arrayed with 45  $\mu\text{m}$  period, 15  $\mu\text{m}$  base width, and 10  $\mu\text{m}$  height. The overall size of the PDMS stamp is 2.5 mm  $\times$  2.5 mm, which is slightly larger than the membrane to facilitate the transfer printing. In the retrieval step, the PDMS stamp is pressed into full contact with the membrane so that all the pyramids collapse, leading to the maximized contact area and surface adhesion. Then the stamp is retracted rapidly to break the supporting beams and peel off the membrane. Meanwhile, the waveguides can remain intact thanks to the supporting SWGs (Figure S2). After the membrane is picked up, the collapsed pyramids quickly bounce back to the initial state so that only pyramid tips contact the membrane due to the geometry of pyramids and the elastomeric nature of PDMS. As a result, the surface adhesion between stamp and membrane is reduced. In the printing step, the retrieved membrane is pressed into contact with the  $\text{CaF}_2$  substrate but without collapsing the pyramids. Finally, the stamp is retracted slowly, leaving the membrane on the receiver substrate. It is worth noting that this transfer printing technique is capable of integrating virtually any waveguide materials with arbitrary substrate materials. Other waveguide materials such as germanium and aluminum nitride can be combined with various substrate materials (e.g.,  $\text{BaF}_2$ , chalcogenide glasses) to extend the working wavelength to above 8  $\mu\text{m}$ . After the membrane transfer, a 5 nm thick aluminum oxide ( $\text{Al}_2\text{O}_3$ ) layer is deposited by atomic layer deposition (ALD) to electrically isolate graphene and Si waveguide. While  $\text{Al}_2\text{O}_3$  is lossy in the LWIR, the additional loss caused by such a thin  $\text{Al}_2\text{O}_3$  layer is negligible. The van der Waals force between the Si membrane and the  $\text{CaF}_2$  substrate is strong enough for the following graphene transfer and

electrode lift-off steps, as shown in Figure 2d,e, respectively. Details on these two steps are given in Figure S3.

**Transfer-Printed Waveguides.** The fundamental performances of transfer-printed SOCF waveguides, including propagation loss, bending loss, and Y-junction, are characterized in the broad LWIR wavelength range from 6.3 to 7.1  $\mu\text{m}$ , which is covered by two different grating coupler designs (GC I and GC II; see Figure S4 for details). The scanning electron microscope (SEM) images of the waveguide, 90° bend, and Y-junction are shown in Figure 3a–c, whereas their overall optical microscope (OM) images are shown in Figure S5a–c. Waveguides with different lengths are fabricated on the same membrane for cut-back measurement of propagation loss (Figure S5a). The waveguide width  $W$ , SWG cladding width  $W_{\text{SWG}}$ , and Si strip length  $L_{\text{Si}}$  in the SWG cladding are 3.1, 3.35, and 0.38  $\mu\text{m}$ , respectively. The SWG period  $\Lambda_{\text{SWG}}$  of 1  $\mu\text{m}$  is smaller than the Bragg period of  $\sim 1.15$   $\mu\text{m}$ , enabling the SWG waveguides to behave similarly to normal strip waveguides with low propagation loss. As shown in Figure 3d, an average propagation loss of 4.64 dB/cm is measured with a standard deviation of 0.51 dB/cm. The propagation loss is mainly attributed to the scattering from the waveguide surface roughness. Similarly, waveguides with different 90° bend numbers are fabricated on the same membrane for bending loss measurement (Figure S5b). The radius of each bend is 35  $\mu\text{m}$ . Figure 3e shows a bending loss of  $0.054 \pm 0.005$  dB/90°, about half of which comes from the propagation loss in the bend and the other half mainly the mode mismatch loss between the bend and the straight section. The Y-junction is designed with  $x$ - and  $y$ -spans of 307 and 288  $\mu\text{m}$ , respectively. The Y-junction performance is characterized by measuring the output from four cascaded Y-junctions (Figure S5c). The transmission is  $-3.42 \pm 0.27$  dB/port, as shown in Figure 3f, confirming a broadband 50:50 light splitting ratio and a low insertion loss of  $\sim 0.42$  dB. The insets in Figure 3d–f are representative fitting results of measured cut-back data at 6.55  $\mu\text{m}$ , demonstrating good linearity.

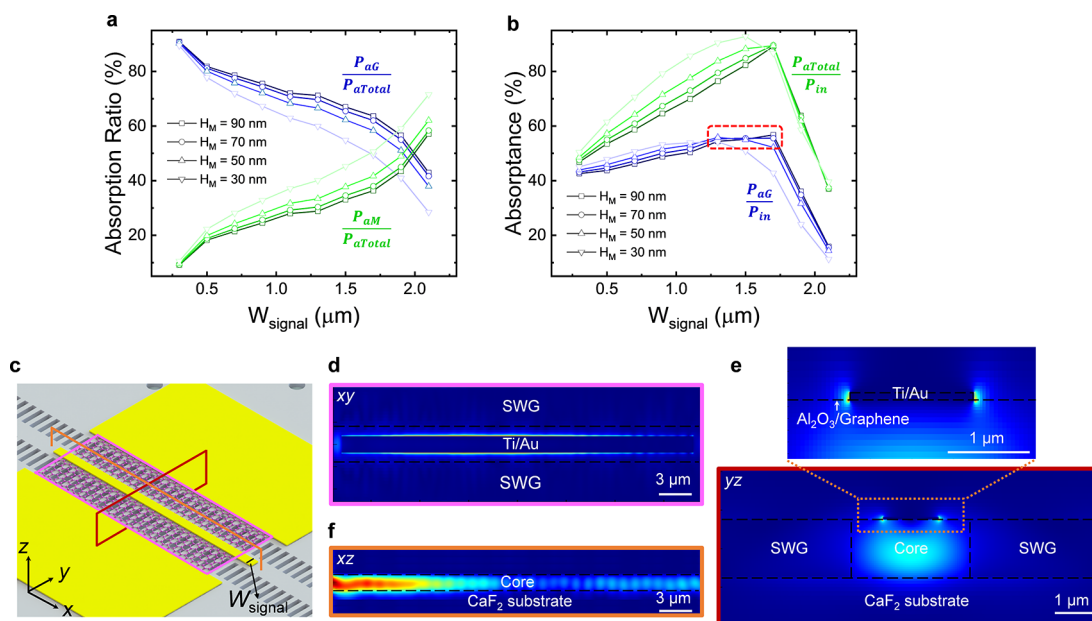


**Figure 4.** Design of waveguide-integrated graphene photodetector. (a) Power absorption ratios of graphene and metal at different widths and thicknesses of the signal electrode. (b) Graphene and total absorptances at different widths and thicknesses of the signal electrode. (c) Schematic illustration of the simulated structure. Electric field  $|E_y|$  distribution in the (d)  $xy$ , (e)  $yz$ , and (f)  $xz$  planes.

**Photodetector Design.** In addition to enabling zero-bias photocarrier separation and collection, the middle signal electrode also provides plasmonic enhancement. The electric field near the signal electrode is enhanced by two mechanisms. The first mechanism is plasmon-induced field localization, which is a result of the continuity of boundary conditions in Maxwell equations.<sup>47</sup> At the interface of two materials, electrical displacements on both sides should be equal,  $D_1 = D_2$ . Because  $D = \epsilon E$ , the electric field  $E$  will be much larger in the material with a smaller dielectric constant  $\epsilon$ . The second mechanism is plasmonic resonance.<sup>48</sup> With a properly designed width of the signal electrode, the transverse component  $E_y$  of the waveguide mode in Si underneath can be efficiently coupled to the plasmonic resonance of the metallic electrode. Figure S6 shows the  $E_y$  real part distribution at the waveguide cross section. A plasmonic resonance can be observed. Such a resonance is localized surface plasmon resonance and leads to electric field enhancement as two hot spots at both sides of the electrode. The enhanced electric field overlaps with the metal-doped graphene junctions, leading to a significant performance improvement of the graphene photodetector.

The geometric parameters of the signal electrode have a decisive impact on photodetector performance. A trade-off needs to be considered between plasmonic enhancement and metal absorption. The graphene and metal absorptions are simulated using the finite-difference time-domain (FDTD) method. The length of transferred graphene flake on waveguide is 33  $\mu\text{m}$ . The graphene is described by a 2D conductive model,<sup>49</sup> in which the conductivity is scaled by the number of layers according to the flake thickness measured by atomic force microscopy (AFM) (Figure S7). The total absorption is calculated by comparing the transmission in all the directions with input unity power, while graphene absorption is calculated by

$$P_{aG} = \frac{1}{2} \iint \text{Real}(\sigma_G) |E|^2 dS \quad (1)$$

in which  $\text{Real}(\sigma_G)$  is the real part of the graphene conductivity,  $E$  is the electric field at the graphene surface, and  $S$  is the graphene area on the waveguide. Figure 4a shows how the width  $W_{\text{signal}}$  and thickness  $H_M$  of signal electrode affect the ratios of graphene and metal absorptions over the total absorption. A wider and thinner signal electrode makes the metal absorption more dominant, reducing the graphene absorption ratio  $\frac{P_{aG}}{P_{aTotal}}$ . This trend agrees with the reported results.<sup>41,44</sup> For a higher responsivity, graphene is desired to absorb more than metal, necessitating a narrower and thicker signal electrode, which, however, also decreases their absorptions. To have a better design guideline, in Figure 4b, the graphene and total absorbed powers are compared with the incident power. The total absorptance  $\frac{P_{aTotal}}{P_{in}}$  increases with  $W_{\text{signal}}$ , reaching 90% at 1.7  $\mu\text{m}$  but drops dramatically when it is further widened. This is because plasmonic resonance is strongest only when  $W_{\text{signal}}$  matches working wavelength, leading to highest local electric field enhancement (Figure S8). Correspondingly, the graphene absorptance  $\frac{P_{aG}}{P_{in}}$  is also improved from  $\sim 43$  to  $\sim 55\%$  with  $W_{\text{signal}}$  increasing from 0.3 to 1.7  $\mu\text{m}$ . With  $W_{\text{signal}}$  narrower than 1.7  $\mu\text{m}$ , the graphene and total absorptances can also be enhanced by reducing the metal thickness.  $\frac{P_{aG}}{P_{in}}$  reaches maximum and is nearly constant when  $W_{\text{signal}}$  and  $H_M$  range from 1.3 to 1.7  $\mu\text{m}$  and from 50 to 90 nm, respectively.  $W_{\text{signal}}$  and  $H_M$  are chosen to be 1.5  $\mu\text{m}$  and 70 nm, respectively, for better fabrication tolerance. With these parameters, the simulated total and graphene absorptances reach 85 and 55%, respectively. The graphene absorption can be further enhanced by fabricating the waveguide with a thinner Si device layer, so as to expose a larger fraction of the waveguide modal field to the graphene.<sup>44</sup> Since the Si waveguide directly sits on the bulk LWIR-transparent  $\text{CaF}_2$  substrate, our SOCF platform is free from the substrate leakage issue suffered by SOI and suspended Si platforms, enabling the

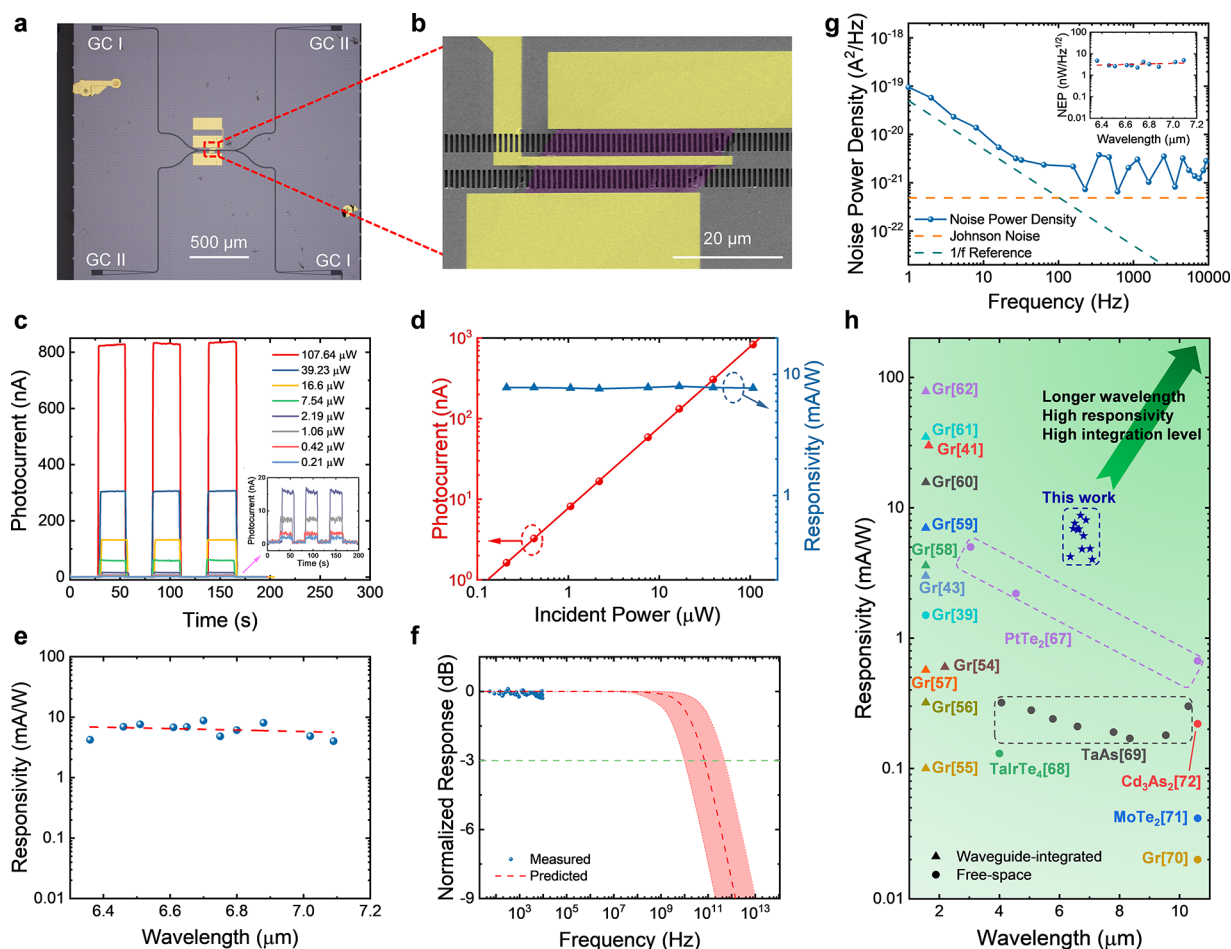


**Figure 5.** Photodetector characterization. (a) OM image of the graphene photodetector integrated with SOCF waveguide featuring two grating couplers with different designs for broadband characterization. (b) False-colored SEM image of the waveguide-integrated graphene photodetector: graphene in purple and electrodes in yellow. (c) Temporal photoresponses under different incident powers. Inset shows the results under low incident powers. (d) Photocurrent and responsivity as a function of incident power. (e) Spectral responsivity. (f) Measured and predicted frequency response. Red shaded area denotes the range of reported data and hence the uncertainty of our estimation. (g) Spectral current noise power density. Inset: Spectral NEP. (h) Comparison with previously reported semimetal photodetectors at zero bias. A small bias of 100  $\mu\text{V}$  was applied to the TaAs photodetector.<sup>69</sup>

use of a small waveguide thickness down to a few hundred nanometers. Nonetheless, a comprehensive consideration on four factors, namely, absorption loss, scattering loss, mechanical robustness, and membrane size, is needed when choosing the waveguide thickness (Note S9).

The electric field distribution is simulated with the chosen parameters (1.5  $\mu\text{m}$   $W_{\text{signal}}$  and 70 nm  $H_{\text{M}}$ ) at three coordinate hyperplanes, as shown in Figure 4c. In the  $xy$  plane, where the graphene is placed, the electric field is enhanced in the vicinity of the signal electrode, which can also be observed in the  $yz$  plane. In the  $xz$  plane, the waveguide mode is absorbed by 66% within the first 20  $\mu\text{m}$  propagation length and then saturates. It should be also noted that, although Figure 4d–f presents field distribution at 6.51  $\mu\text{m}$ , the electric field remains nearly unchanged across the whole working range from 6.3 to 7.1  $\mu\text{m}$ , as shown in Figure S11. A broadband plasmonic enhancement, and thus a nearly flat spectral responsivity, can be expected.

**Photodetector Characterization.** Figure 5a shows the OM image of the fabricated waveguide-integrated graphene photodetector. GC I and GC II are combined through a Y-junction to couple the broadband light into the graphene photodetector. The residual light is split by another Y-junction and coupled out by another pair of GC I and GC II to facilitate

the optical alignment. Figure 5b presents the false-colored SEM image of the photodetector. The photodetector performance is characterized at zero bias. A lock-in amplifier technique is utilized to improve the signal-to-noise ratio (SNR). The laser beam is modulated by an optical chopper at 227 Hz. The lock-in amplifier collects the photocurrent at the same frequency. The incident power onto the photodetector is calibrated according to the insertion loss from the input grating coupler to the photodetector. This loss is obtained with the assistance of a simultaneously fabricated reference chip with an identical waveguide structure but without photodetector integrated. Because the photodetector is integrated on the center of the whole symmetric waveguide structure, this loss can be conveniently extracted by halving the total on-chip insertion losses measured by the reference chip. Figure 5c shows the temporal responses under different incident powers ranging from 0.21 to 107.64  $\mu\text{W}$  at 6.51  $\mu\text{m}$ . The inset shows the zoom-in view of photoresponses under low incident powers. The highly repeatable photocurrent generation reveals stable and reversible photoresponse in our device. The photocurrents are extracted from Figure 5c and plotted as a function of the incident power in Figure 5d. It is seen that the photocurrent almost increases linearly with increasing incident power.

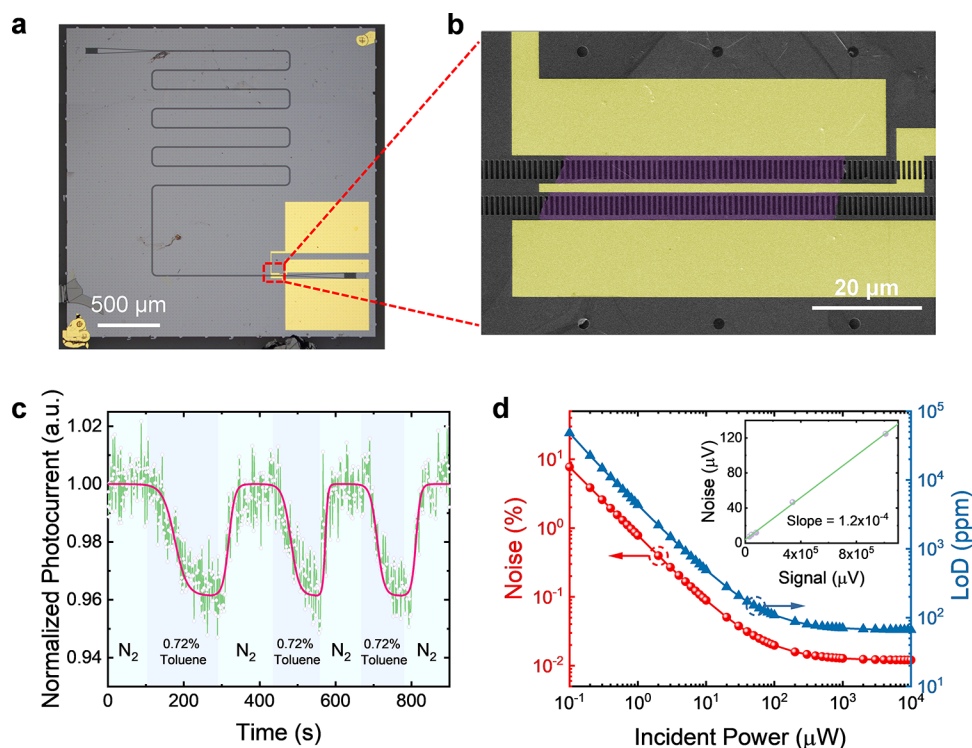


**Figure 6.** On-chip sensing demonstration. (a) OM image of the graphene photodetector integrated with SOCF folded waveguide. (b) False-colored SEM image of the waveguide-integrated graphene photodetector: graphene in purple and electrodes in yellow. (c) Photoresponse of the waveguide-integrated graphene photodetector under alternating injection of pure  $N_2$  and 0.72% toluene– $N_2$  dilution into the vicinity of the folded waveguide. (d) Noise and LoD as a function of the incident power to the waveguide-integrated graphene photodetector. Inset: Noise as a function of the signal measured by the MCT detector. The slope of the linear fitting suggests a laser power fluctuation of 0.012% of the signal.

Correspondingly, the responsivity (responsivity =  $I_{ph}/P$ ) is power-independent and calculated to be  $\sim 7.8$  mA/W. Photoresponses are then measured at different LWIR wavelengths. As shown in Figure 5e, our device possesses broadband photoresponse from 6.3 to 7.1  $\mu\text{m}$ . As expected, the responsivity does not show significant wavelength dependence. The frequency response is examined by adjusting the optical chopper modulation frequency, which is up to 10 kHz. Within this measurable range, the photoresponse does not show any noticeable degradation, implying a far larger bandwidth of our device, as illustrated in Figure 5f. Because the photocurrent is generated near the graphene/metal interfaces by PV and PTE effects, the 3 dB bandwidth of our device is predicted to range from 10 to 500 GHz.<sup>38–40,50,51</sup>

The noise of the device is further measured using a lock-in amplifier in dark condition. Because zero-bias operation eliminates the dark current-induced shot noise, the noise mainly consists of  $1/f$  noise and Johnson noise. As shown in Figure 5g, at frequencies below  $\sim 100$  Hz, the measured noise power density spectrum is parallel to the  $1/f$  reference line, indicating the noise is dominated by the  $1/f$  noise. At higher frequencies, Johnson noise  $i_j$  becomes dominant, which is calculated from the measured resistance  $R$  of the device (extracted from the  $I$ – $V$  curve as shown in Figure S12) according to

$$(i_j)^2 = 4k_B T \Delta f / R \quad (2)$$

where  $k_B$  is the Boltzmann constant,  $T$  is the temperature, and  $\Delta f$  is the bandwidth. Because our device can operate at speeds well beyond 100 Hz, it is not significantly affected by the large

$1/f$  noise at low frequencies. The  $\sim 150 \Omega$  resistance and, as a result, the noise of our device are at the same level as those of reported works.<sup>44,52,53</sup> The noise equivalent power,  $NEP = \frac{\sqrt{\text{noise power density}}}{\text{responsivity}}$ , as a function of wavelength is calculated and plotted in the inset of Figure 5g. The NEP ranges from 2.3 to 5.0 nW/Hz<sup>1/2</sup> across the 6.3–7.1  $\mu\text{m}$  wavelength range.

In Figure 5h, we compare the responsivity of our device with those of reported semimetal photodetectors under zero-bias operation. Most of the reported waveguide-integrated graphene photodetectors operate in the NIR.<sup>41,43,54–62</sup> When migrating to the much longer wavelengths in the LWIR, the photon energy becomes significantly lower and the graphene absorption is largely suppressed.<sup>45</sup> Thanks to the maximized plasmonic enhancement by signal electrode optimization, our device realizes responsivities comparable with those working in the NIR. Currently, the responsivity of our device is mainly limited by three factors. First is the lack of gate tuning. Thus, we are not able to electrically adjust the graphene chemical potential of the as-fabricated device. Gate tuning of graphene chemical potential results in the change of its Seebeck coefficient and absorption, offering more opportunities for photoresponse optimization.<sup>58,61,62</sup> The gate tuning can be enabled by depositing a gate dielectric layer and fabricating a gate electrode on top,<sup>58</sup> by spin-coating a polymer electrolyte layer,<sup>62</sup> or by using the Si waveguide as a back gate when the Si is doped with a moderate resistivity.<sup>61</sup> Second is the efficiency of photocarrier transport. The size of the plasmonic hot spots scales with wavelength, while that of the metal-doped graphene

junctions does not, resulting in less efficient photocarrier separation and collection in our device as compared with the NIR counterpart employing a similar plasmonic enhancement strategy (Note S12).<sup>41</sup> This limiting factor could be relieved by modulating the potential distribution by a gate.<sup>58,62</sup> Moreover, a split-gate geometry can be employed for metallic top gate<sup>42</sup> or waveguide back gate.<sup>61</sup> The split gates create a tunable p–n junction by applying two different gate voltages and simultaneously concentrate the optical field in the slot, that is, exactly in between the p- and n-doped regions, maximizing the photoresponse. Third is the impurities and defects in the graphene, which reduce the carrier mobility and thus the photodetector responsivity. The impurities and defects could be reduced by optimizing the fabrication process with less contamination and strain,<sup>63,64</sup> cleaning the graphene surface by a postprocess such as thermal annealing or ozone treatment,<sup>65,66</sup> and encapsulating graphene in hexagonal boron nitride.<sup>62</sup> With these improvement efforts, an even higher responsivity would be expected.

In addition to graphene, various semimetals are being investigated to construct IR photodetectors with free-space geometry.<sup>39,67–72</sup> Compared with them, our device achieves superior responsivities with much thinner photodetection material thickness as powered by the waveguide integration. Some of these emerging semimetals are also with 2D layered lattice structures, whose integrations with waveguides have not been explored yet. Our demonstrated LWIR waveguide-integrated graphene photodetector provides a potential solution for high responsivity photodetectors at longer wavelengths, as well as for on-chip spectroscopic sensing.<sup>73</sup>

**Sensing Demonstration.** In order to evaluate the feasibility of utilizing this waveguide-integrated photodetector for on-chip LWIR absorption sensing, another graphene photodetector based on the same concept is integrated with a SOCF folded waveguide, as shown in Figure 6a. The folded geometry offers a long light–matter interaction length of 1.1 cm within the small footprint of the membrane. As shown in Figure 6b, this photodetector also employs GSG electrode configuration. The signal electrode width is optimized using the same FDTD simulation method according to the AFM-measured flake thickness (see Figure S14 for details). Light of 6.65  $\mu\text{m}$  wavelength from a tunable LWIR laser is modulated at 227 Hz and grating-coupled to the folded waveguide sensing element. Figure 6c presents the measured photoresponse of the waveguide-integrated graphene photodetector when pure nitrogen ( $\text{N}_2$ ) and 0.72% toluene– $\text{N}_2$  dilution are alternately injected into the vicinity of the folded waveguide. A clear and repeatable drop of the photocurrent is observed under the injection of toluene. The 0.72% toluene leads to  $\sim 3.86\%$  photocurrent decrease. The waveguide sensor follows Beer's law:

$$T = I_{\text{toluene}}/I_{\text{no toluene}} = \exp(-\alpha\Gamma LC) \quad (3)$$

where  $T$  is the transmittance,  $I_{\text{toluene}}$  is the detector signal under a toluene– $\text{N}_2$  mixture,  $I_{\text{no toluene}}$  is the detector signal under pure  $\text{N}_2$ ,  $\alpha$  is the absorption coefficient of pure toluene,  $\Gamma$  is the waveguide mode confinement factor in the analyte (which is 7.12% based on our modal simulation),  $L$  is the length of the folded waveguide sensing element, and  $C$  is the toluene volumetric concentration. According to the 0.72% toluene sensing result,  $\alpha$  is calculated to be  $69.71 \text{ cm}^{-1}$ . It is also read from Figure 6c that noise is about 0.87% of the photocurrent. Adopting the common criterion of  $\text{SNR} = 3$ , an LoD of 0.48%

is derived. Our experimentally demonstrated LoD is slightly better than the 1% LoD achieved by the previously reported on-chip MWIR gas sensor featuring chalcogenide waveguide integrated with a PbTe photodetector.<sup>74</sup> The measured noise mainly consists of graphene photodetector noise and laser power fluctuation. The laser power fluctuation is assessed using a free-space liquid- $\text{N}_2$ -cooled MCT detector, as plotted in the inset of Figure 6d. The slope of the linear fitting suggests that the laser power fluctuation occupies 0.012% of the signal. Therefore, most of the measured 0.87% noise is attributed to the noise of the graphene photodetector, which is constant and does not scale up with the signal level. By optimizing the loss from the laser to the graphene photodetector or increasing the laser power, the incident power to the graphene photodetector could be increased, making the laser power fluctuation more dominant. As a result, with the increase of incident power, the noise percentage could decrease and a lower LoD is expected, as illustrated in Figure 6d. In addition to the demonstration of toluene sensing, it is worth highlighting here that the presented system would have broad applicability in LWIR spectroscopic sensing due to its broadband behavior and the inherent selectivity of LWIR absorption spectroscopy.

## CONCLUSION

In conclusion, we have demonstrated LWIR heterogeneously integrated graphene/Si/CaF<sub>2</sub> waveguide photodetectors with zero standby power consumption. A simple transfer printing method based on microstructured PDMS stamps is developed for the high-yield fabrication of SOCF waveguides. The transfer-printed SOCF waveguides show low propagation loss, bending loss, and Y-junction insertion loss in the broad wavelength range from 6.3 to 7.1  $\mu\text{m}$ . Through waveguide integration and plasmonic enhancement, a high and broadband responsivity of around 8 mA/W is achieved in the graphene photodetector under zero-bias operation. The waveguide-integrated graphene photodetector is further utilized for on-chip absorption sensing. Detection of 0.72% toluene is experimentally demonstrated, better than the LoD achieved by the previously reported MWIR chalcogenide waveguide sensor integrated with an on-chip PbTe photodetector. Our technology could be potentially employed to realize chip-scale LWIR spectroscopic sensing systems.

## METHODS

**Fabrication.** The fabrication started from an SOI wafer with a 1.5  $\mu\text{m}$  thick device layer and a 3  $\mu\text{m}$  thick BOX layer. The waveguide and membrane patterns were simultaneously defined by e-beam lithography (EBL) (Jeol JBX-6300FS) using ZEP-520A resist and then transferred to the Si device layer by SF<sub>6</sub>/C<sub>4</sub>F<sub>8</sub> deep reactive-ion etching (Oxford Plasmalab System 100). The wafer was then submerged into a 1:5 HF bath for 3.5 h to ensure removal of the BOX beneath the widest devices. The wafer was slowly dried using CPD (Leica EM CPD300) to avoid any damage to the membranes. The membranes were then transfer-printed onto CaF<sub>2</sub> substrates by PDMS stamps as described above. The preparation method for the PDMS stamps is depicted in Note S1. The residual ZEP-520A resist was removed by first acetone bath then oxygen plasma etching (SPI Plasma Prep III). A 5 nm thick Al<sub>2</sub>O<sub>3</sub> layer was then deposited by ALD (Cambridge NanoTech Savannah) for electrical isolation. Exfoliated graphene flakes were transferred onto the waveguides with the method described in Note S3. Electrodes were patterned by another EBL step with poly(methyl methacrylate) (PMMA) as resist. Subsequently, 1 nm Ti and 70 nm Au were deposited by e-beam evaporation (AJA), followed by lift-off in acetone.

**Characterization.** A continuous-wave laser (Daylight Solutions MIRcat-2300) was modulated by an optical chopper (Stanford Research Systems SR540) and launched into a hollow fiber (Opto-Knowledge HF200MWLW-FC) by a ZnSe focusing lens (Innovation Photonics LFO-5-6). The alignment between the fiber and the devices was performed with a six-axis alignment stage (Kohzu). For waveguide characterization, the output light was coupled to another hollow fiber and directed to a liquid-N<sub>2</sub>-cooled MCT detector (InfraRed Associates MCT-13-1.00). Both the chopper and the detector were connected to a lock-in amplifier (Stanford Research Systems SR830) to enhance the SNR. For the characterization of graphene photodetectors, the waveguide characterization setup was maintained to assist the optical alignment. The photoresponse signals from the graphene photodetectors were collected by another lock-in amplifier. In the power dependence measurement, the light intensity was adjusted by neutral density filters (Thorlabs NDIR03A, NDIR10A, NDIR20A; Edmund Optics LWIR 0.7OD) and calibrated with a power meter (Newport 843-R). The *I*–*V* curves were measured with a semiconductor characterization system (Keithley 4200-SCS). For the toluene sensing characterization, N<sub>2</sub> was selected as the diluting gas with its overall flow rate controlled by a mass flow controller. This diluting gas was divided into two flows, with one pumped into 99.5% toluene solution to generate a toluene–N<sub>2</sub> mixture, and the other remained as pure N<sub>2</sub>. After that, the two flows were remixed, and the toluene concentration in the dilution was calibrated by a commercial sensor before pumped into the gas feeding chamber. The concentration of toluene in the sensing region was precisely and dynamically controlled by regulating the valves in the two flows. The setup for all three characterizations above is schematically illustrated in Figure S15. All measurements were performed at room temperature.

## ASSOCIATED CONTENT

### Supporting Information

The Supporting Information is available free of charge at <https://pubs.acs.org/doi/10.1021/acsnano.1c01859>.

PDMS stamp fabrication process; membrane retrieval by PDMS stamp; graphene photodetector integration process; two grating coupler designs; transfer-printed waveguides; illustration of plasmonic resonance; Raman and AFM measurements; electric field distributions with different signal electrode widths; discussion on waveguide thickness; electric field distributions at different wavelengths; graphene photodetector *I*–*V* curve; plasmonic hot spots at different wavelengths; graphene photodetector for sensing demonstration; measurement setup (PDF)

## AUTHOR INFORMATION

### Corresponding Author

**Chengkuo Lee** – Department of Electrical and Computer Engineering, National University of Singapore, Singapore 117583; Center for Intelligent Sensors and MEMS (CISM), National University of Singapore, Singapore 117608; NUS Suzhou Research Institute (NUSRI), Suzhou 215123, China; NUS Graduate School - Integrative Sciences and Engineering Programme (ISEP), National University of Singapore, Singapore 119077; [orcid.org/0000-0002-8886-3649](https://orcid.org/0000-0002-8886-3649); Email: [lelelc@nus.edu.sg](mailto:lelelc@nus.edu.sg)

### Authors

**Yiming Ma** – Department of Electrical and Computer Engineering, National University of Singapore, Singapore 117583; Center for Intelligent Sensors and MEMS (CISM), National University of Singapore, Singapore 117608; NUS

Suzhou Research Institute (NUSRI), Suzhou 215123, China; [orcid.org/0000-0002-5730-3956](https://orcid.org/0000-0002-5730-3956)

**Yuhua Chang** – Department of Electrical and Computer Engineering, National University of Singapore, Singapore 117583; Center for Intelligent Sensors and MEMS (CISM), National University of Singapore, Singapore 117608; [orcid.org/0000-0003-0337-1934](https://orcid.org/0000-0003-0337-1934)

**Bowei Dong** – Department of Electrical and Computer Engineering, National University of Singapore, Singapore 117583; Center for Intelligent Sensors and MEMS (CISM), National University of Singapore, Singapore 117608

**Jingxuan Wei** – Department of Electrical and Computer Engineering, National University of Singapore, Singapore 117583; Center for Intelligent Sensors and MEMS (CISM), National University of Singapore, Singapore 117608; [orcid.org/0000-0003-0295-3764](https://orcid.org/0000-0003-0295-3764)

**Weixin Liu** – Department of Electrical and Computer Engineering, National University of Singapore, Singapore 117583; Center for Intelligent Sensors and MEMS (CISM), National University of Singapore, Singapore 117608

Complete contact information is available at: <https://pubs.acs.org/doi/10.1021/acsnano.1c01859>

### Author Contributions

Y.M. and Y.C. contributed equally. C.L. supervised the project. Y.M. and Y.C. carried out the device fabrication and characterization. Y.M., Y.C., and B.D. built up the waveguide and photodetector characterization setup. Y.M., Y.C., and J.W. performed the simulation and analysis. Y.M., Y.C., and W.L. performed the sensing demonstration. Y.M., Y.C., and C.L. drafted the manuscript. All authors discussed the results and contributed to the preparation of the manuscript.

### Funding

This research is supported by the National Research Foundation Competitive Research Programme (NRF-CRP15-2015-02) and the NRF-ISF Joint Research Grant (NRF2015-NRF-ISF001-2620).

### Notes

The authors declare no competing financial interest.

### ACKNOWLEDGMENTS

The authors thank Jun You Tan from Centre for Advanced 2D Materials, National University of Singapore for the kind help and fruitful discussion.

### REFERENCES

- Schliesser, A.; Picqué, N.; Hänsch, T. W. Mid-Infrared Frequency Combs. *Nat. Photonics* **2012**, *6*, 440–449.
- Ycas, G.; Giorgetta, F. R.; Baumann, E.; Coddington, I.; Herman, D.; Diddams, S. A.; Newbury, N. R. High-Coherence Mid-Infrared Dual-Comb Spectroscopy Spanning 2.6 to 5.2  $\mu\text{m}$ . *Nat. Photonics* **2018**, *12*, 202–208.
- Dam, J. S.; Tidemand-Lichtenberg, P.; Pedersen, C. Room-Temperature Mid-Infrared Single-Photon Spectral Imaging. *Nat. Photonics* **2012**, *6*, 788–793.
- Liu, X.; Kuyken, B.; Roelkens, G.; Baets, R.; Osgood, R. M.; Green, W. M. J. Bridging the Mid-Infrared-to-Telecom Gap with Silicon Nanophotonic Spectral Translation. *Nat. Photonics* **2012**, *6*, 667–671.
- Vlk, M.; Datta, A.; Alberti, S.; Yallev, H. D.; Mittal, V.; Murugan, G. S.; Jágorská, J. Extraordinary Evanescent Field Confinement Waveguide Sensor for Mid-Infrared Trace Gas Spectroscopy. *Light: Sci. Appl.* **2021**, *10*, 26.

- (6) Yang, Z.; Albrow-Owen, T.; Cai, W.; Hasan, T. Miniaturization of Optical Spectrometers. *Science* **2021**, *371*, No. eabe0722.
- (7) Zheng, S. N.; Zou, J.; Cai, H.; Song, J. F.; Chin, L. K.; Liu, P. Y.; Lin, Z. P.; Kwong, D. L.; Liu, A. Q. Microring Resonator-Assisted Fourier Transform Spectrometer with Enhanced Resolution and Large Bandwidth in Single Chip Solution. *Nat. Commun.* **2019**, *10*, 2349.
- (8) Lin, H.; Luo, Z.; Gu, T.; Kimerling, L. C.; Wada, K.; Agarwal, A.; Hu, J. Mid-Infrared Integrated Photonics on Silicon: A Perspective. *Nanophotonics* **2017**, *7*, 393–420.
- (9) Kozak, D. A.; Stievater, T. H.; Mahon, R.; Rabinovich, W. S. Germanium-on-Silicon Waveguides at Wavelengths from 6.85 to 11.25 Microns. *IEEE J. Sel. Top. Quantum Electron.* **2018**, *24*, 8200804.
- (10) Nader, N.; Kowligy, A.; Chiles, J.; Stanton, E. J.; Timmers, H.; Lind, A. J.; Cruz, F. C.; Lesko, D. M. B.; Briggman, K. A.; Nam, S. W.; Diddams, S. A.; Mirin, R. P. Infrared Frequency Comb Generation and Spectroscopy with Suspended Silicon Nanophotonic Waveguides. *Optica* **2019**, *6*, 1269–1276.
- (11) Dong, B.; Guo, X.; Ho, C. P.; Li, B.; Wang, H.; Lee, C.; Luo, X.; Lo, G. Q. Silicon-on-Insulator Waveguide Devices for Broadband Mid-Infrared Photonics. *IEEE Photonics J.* **2017**, *9*, 4501410.
- (12) Lin, P. T.; Singh, V.; Lin, H. Y. G.; Tiwald, T.; Kimerling, L. C.; Agarwal, A. M. Low-Stress Silicon Nitride Platform for Mid-Infrared Broadband and Monolithically Integrated Microphotonics. *Adv. Opt. Mater.* **2013**, *1*, 732–739.
- (13) Kang, J.; Takenaka, M.; Takagi, S. Novel Ge Waveguide Platform on Ge-on-Insulator Wafer for Mid-Infrared Photonic Integrated Circuits. *Opt. Express* **2016**, *24*, 11855–11864.
- (14) Baehr-Jones, T.; Spott, A.; Ilic, R.; Spott, A.; Penkov, B.; Asher, W.; Hochberg, M. Silicon-on-Sapphire Integrated Waveguides for the Mid-Infrared. *Opt. Express* **2010**, *18*, 12127–12135.
- (15) Khan, S.; Chiles, J.; Ma, J.; Fathpour, S. Silicon-on-Nitride Waveguides for Mid- and Near-Infrared Integrated Photonics. *Appl. Phys. Lett.* **2013**, *102*, 121104.
- (16) Penadés, J. S.; Sánchez-Postigo, A.; Nedeljkovic, M.; Ortega-Moñux, A.; Wangüemert-Pérez, J. G.; Xu, Y.; Halir, R.; Qu, Z.; Khokhar, A. Z.; Osman, A.; Cao, W.; Littlejohns, C. G.; Cheben, P.; Molina-Fernández, I.; Mashanovich, G. Z. Suspended Silicon Waveguides for Long-Wave Infrared Wavelengths. *Opt. Lett.* **2018**, *43*, 795–798.
- (17) Nedeljkovic, M.; Penades, J. S.; Mittal, V.; Murugan, G. S.; Khokhar, A. Z.; Littlejohns, C.; Carpenter, L. G.; Gawith, C. B. E.; Wilkinson, J. S.; Mashanovich, G. Z. Germanium-on-Silicon Waveguides Operating at Mid-Infrared Wavelengths up to 8.5  $\mu\text{m}$ . *Opt. Express* **2017**, *25*, 27431–27441.
- (18) Brun, M.; Labeye, P.; Grand, G.; Hartmann, J.-M.; Boulila, F.; Carras, M.; Nicoletti, S. Low Loss SiGe Graded Index Waveguides for Mid-IR Applications. *Opt. Express* **2014**, *22*, 508–518.
- (19) Park, S.-I.; Xiong, Y.; Kim, R.-H.; Elvikis, P.; Meitl, M.; Kim, D.-H.; Wu, J.; Yoon, J.; Yu, C.-J.; Liu, Z.; Huang, Y.; Hwang, K. - c.; Ferreira, P.; Li, X.; Choquette, K.; Rogers, J. A. Printed Assemblies of Inorganic Light-Emitting Diodes for Deformable and Semitransparent Displays. *Science* **2009**, *325*, 977–981.
- (20) Yuan, H.-C.; Shin, J.; Qin, G.; Sun, L.; Bhattacharya, P.; Lagally, M. G.; Celler, G. K.; Ma, Z. Flexible Photodetectors on Plastic Substrates by Use of Printing Transferred Single-Crystal Germanium Membranes. *Appl. Phys. Lett.* **2009**, *94*, No. 013102.
- (21) Yang, Y.; Hwang, Y.; Cho, H. A.; Song, J. H.; Park, S. J.; Rogers, J. A.; Ko, H. C. Arrays of Silicon Micro/Nanostructures Formed in Suspended Configurations for Deterministic Assembly Using Flat and Roller-Type Stamps. *Small* **2011**, *7*, 484–491.
- (22) Chen, Y.; Lin, H.; Hu, J.; Li, M. Heterogeneously Integrated Silicon Photonics for the Mid-Infrared and Spectroscopic Sensing. *ACS Nano* **2014**, *8*, 6955–6961.
- (23) Hattasan, N.; Gassenq, A.; Cerutti, L.; Rodriguez, J. B.; Tournié, E.; Roelkens, G. Heterogeneous Integration of GaInAsSb *p-i-n* Photodiodes on a Silicon-on-Insulator Waveguide Circuit. *IEEE Photonics Technol. Lett.* **2011**, *23*, 1760–1762.
- (24) Wang, R.; Sprengel, S.; Muneeb, M.; Boehm, G.; Baets, R.; Amann, M.-C.; Roelkens, G. 2  $\mu\text{m}$  Wavelength Range InP-Based Type-II Quantum Well Photodiodes Heterogeneously Integrated on Silicon Photonic Integrated Circuits. *Opt. Express* **2015**, *23*, 26834–26841.
- (25) Muneeb, M.; Vasiliev, A.; Ruocco, A.; Malik, A.; Chen, H.; Nedeljkovic, M.; Penades, J. S.; Cerutti, L.; Rodriguez, J. B.; Mashanovich, G. Z.; Smit, M. K.; Tourni, E.; Roelkens, G. III-V-on-Silicon Integrated Micro - Spectrometer for the 3  $\mu\text{m}$  Wavelength Range. *Opt. Express* **2016**, *24*, 9465–9472.
- (26) Grote, R. R.; Souhan, B.; Ophir, N.; Driscoll, J. B.; Bergman, K.; Bakhru, H.; Green, W. M. J.; Osgood, R. M. Extrinsic Photodiodes for Integrated Mid-Infrared Silicon Photonics. *Optica* **2014**, *1*, 264–267.
- (27) Souhan, B.; Grote, R. R.; Chen, C. P.; Huang, H.-C.; Driscoll, J. B.; Lu, M.; Stein, A.; Bakhru, H.; Bergman, K.; Green, W. M. J.; Osgood, R. M. Si<sup>+</sup>-Implanted Si-Wire Waveguide Photodetectors for the Mid-Infrared. *Opt. Express* **2014**, *22*, 27415–27424.
- (28) Ackert, J. J.; Thomson, D. J.; Shen, L.; Peacock, A. C.; Jessop, P. E.; Reed, G. T.; Mashanovich, G. Z.; Knights, A. P. High-Speed Detection at Two Micrometres with Monolithic Silicon Photodiodes. *Nat. Photonics* **2015**, *9*, 393–396.
- (29) Xia, F.; Wang, H.; Xiao, D.; Dubey, M.; Ramasubramaniam, A. Two-Dimensional Material Nanophotonics. *Nat. Photonics* **2014**, *8*, 899–907.
- (30) Caldwell, J. D.; Aharonovich, I.; Cassabois, G.; Edgar, J. H.; Gil, B.; Basov, D. N. Photonics with Hexagonal Boron Nitride. *Nat. Rev. Mater.* **2019**, *4*, 552–567.
- (31) Liu, Y.; Weiss, N. O.; Duan, X.; Cheng, H.-C.; Huang, Y.; Duan, X. Van der Waals Heterostructures and Devices. *Nat. Rev. Mater.* **2016**, *1*, 16042.
- (32) Xia, F.; Wang, H.; Hwang, J. C. M.; Neto, A. H. C.; Yang, L. Black Phosphorus and Its Isoelectronic Materials. *Nat. Rev. Phys.* **2019**, *1*, 306–317.
- (33) Huang, L.; Dong, B.; Guo, X.; Chang, Y.; Chen, N.; Huang, X.; Liao, W.; Zhu, C.; Wang, H.; Lee, C.; Ang, K.-W. Waveguide-Integrated Black Phosphorus Photodetector for Mid-Infrared Applications. *ACS Nano* **2019**, *13*, 913–921.
- (34) Liu, J.; Xia, F.; Xiao, D.; García de Abajo, F. J.; Sun, D. Semimetals for High-Performance Photodetection. *Nat. Mater.* **2020**, *19*, 830–837.
- (35) Freitag, M.; Low, T.; Zhu, W.; Yan, H.; Xia, F.; Avouris, P. Photocurrent in Graphene Harnessed by Tunable Intrinsic Plasmons. *Nat. Commun.* **2013**, *4*, 1951.
- (36) Yu, X.; Dong, Z.; Yang, J. K. W.; Wang, Q. J. Room-Temperature Mid-Infrared Photodetector Nanostructure. *Optica* **2016**, *3*, 979–984.
- (37) Yuan, S.; Yu, R.; Ma, C.; Deng, B.; Guo, Q.; Chen, X.; Li, C.; Chen, C.; Watanabe, K.; Taniguchi, T.; García de Abajo, F. J.; Xia, F. Room Temperature Graphene Mid-Infrared Bolometer with a Broad Operational Wavelength Range. *ACS Photonics* **2020**, *7*, 1206–1215.
- (38) Xia, F.; Mueller, T.; Lin, Y. M.; Valdes-Garcia, A.; Avouris, P. Ultrafast Graphene Photodetector. *Nat. Nanotechnol.* **2009**, *4*, 839–843.
- (39) Mueller, T.; Xia, F.; Avouris, P. Graphene Photodetectors for High-Speed Optical Communications. *Nat. Photonics* **2010**, *4*, 297–301.
- (40) Gabor, N. M.; Song, J. C. W.; Ma, Q.; Nair, N. L.; Taychatanapat, T.; Watanabe, K.; Taniguchi, T.; Levitov, L. S.; Jarillo-Herrero, P. Hot Carrier-Assisted Intrinsic Photoresponse in Graphene. *Science* **2011**, *334*, 648–652.
- (41) Pospischil, A.; Humer, M.; Furchi, M. M.; Bachmann, D.; Guider, R.; Fromherz, T.; Mueller, T. CMOS-Compatible Graphene Photodetector Covering All Optical Communication Bands. *Nat. Photonics* **2013**, *7*, 892–896.
- (42) Muench, J. E.; Ruocco, A.; Giambra, M. A.; Miseikis, V.; Zhang, D.; Wang, J.; Watson, H. F. Y.; Park, G. C.; Akhavan, S.; Sorianello, V.; Midrio, M.; Tomadin, A.; Coletti, C.; Romagnoli, M.; Ferrari, A. C.; Goykhman, I. Waveguide-Integrated, Plasmonic Enhanced Graphene Photodetectors. *Nano Lett.* **2019**, *19*, 7632–7644.

- (43) Ma, P.; Salamin, Y.; Baeuerle, B.; Josten, A.; Heni, W.; Emboras, A.; Leuthold, J. Plasmonically Enhanced Graphene Photodetector Featuring 100 Gbit/s Data Reception, High Responsivity, and Compact Size. *ACS Photonics* **2019**, *6*, 154–161.
- (44) Guo, J.; Li, J.; Liu, C.; Yin, Y.; Wang, W.; Ni, Z.; Fu, Z.; Yu, H.; Xu, Y.; Shi, Y.; Ma, Y.; Gao, S.; Tong, L.; Dai, D. High-Performance Silicon–Graphene Hybrid Plasmonic Waveguide Photodetectors beyond 1.55  $\mu\text{m}$ . *Light: Sci. Appl.* **2020**, *9*, 29.
- (45) Xia, F.; Yan, H.; Avouris, P. The Interaction of Light and Graphene: Basics, Devices, and Applications. *Proc. IEEE* **2013**, *101*, 1717–1731.
- (46) Khomyakov, P. A.; Starikov, A. A.; Brocks, G.; Kelly, P. J. Nonlinear Screening of Charges Induced in Graphene by Metal Contacts. *Phys. Rev. B: Condens. Matter Mater. Phys.* **2010**, *82*, 115437.
- (47) Saleh, B. E. A.; Teich, M. C. *Electromagnetic Optics. In Fundamentals of Photonics*; Goodman, J. W., Ed.; John Wiley & Sons, Ltd.: New York, 1991; pp 157–192.
- (48) Pala, R. A.; White, J.; Barnard, E.; Liu, J.; Brongersma, M. L. Design of Plasmonic Thin-Film Solar Cells with Broadband Absorption Enhancements. *Adv. Mater.* **2009**, *21*, 3504–3509.
- (49) Hanson, G. W. Dyadic Green's Functions and Guided Surface Waves for a Surface Conductivity Model of Graphene. *J. Appl. Phys.* **2008**, *103*, No. 064302.
- (50) Sun, D.; Aivazian, G.; Jones, A. M.; Ross, J. S.; Yao, W.; Cobden, D.; Xu, X. Ultrafast Hot-Carrier-Dominated Photocurrent in Graphene. *Nat. Nanotechnol.* **2012**, *7*, 114–118.
- (51) Urich, A.; Unterrainer, K.; Mueller, T. Intrinsic Response Time of Graphene Photodetectors. *Nano Lett.* **2011**, *11*, 2804–2808.
- (52) Wei, J.; Li, Y.; Wang, L.; Liao, W.; Dong, B.; Xu, C.; Zhu, C.; Ang, K.; Qiu, C.; Lee, C. Zero-Bias Mid-Infrared Graphene Photodetectors with Bulk Photoresponse and Calibration-Free Polarization Detection. *Nat. Commun.* **2020**, *11*, 6404.
- (53) Gao, Y.; Zhou, G.; Zhao, N.; Tsang, H. K.; Shu, C. High-Performance Chemical Vapor Deposited Graphene-on-Silicon Nitride Waveguide Photodetectors. *Opt. Lett.* **2018**, *43*, 1399–1402.
- (54) Lin, H.; Song, Y.; Huang, Y.; Kita, D.; Deckoff-Jones, S.; Wang, K.; Li, L.; Li, J.; Zheng, H.; Luo, Z.; Wang, H.; Novak, S.; Yadav, A.; Huang, C.-C.; Shiue, R.-J.; Englund, D.; Gu, T.; Hewak, D.; Richardson, K.; Kong, J.; Hu, J. Chalcogenide Glass-on-Graphene Photonics. *Nat. Photonics* **2017**, *11*, 798–805.
- (55) Wang, J.; Cheng, Z.; Chen, Z.; Xu, J.-B.; Tsang, H. K.; Shu, C. Graphene Photodetector Integrated on Silicon Nitride Waveguide. *J. Appl. Phys.* **2015**, *117*, 144504.
- (56) Gao, Y.; Tao, L.; Tsang, H. K.; Shu, C. Graphene-on-Silicon Nitride Waveguide Photodetector with Interdigital Contacts. *Appl. Phys. Lett.* **2018**, *112*, 211107.
- (57) Gao, Y.; Tsang, H. K.; Shu, C. A Silicon Nitride Waveguide-Integrated Chemical Vapor Deposited Graphene Photodetector with 38 GHz Bandwidth. *Nanoscale* **2018**, *10*, 21851–21856.
- (58) Youngblood, N.; Anugrah, Y.; Ma, R.; Koester, S. J.; Li, M. Multifunctional Graphene Optical Modulator and Photodetector Integrated on Silicon Waveguides. *Nano Lett.* **2014**, *14*, 2741–2746.
- (59) Schall, D.; Neumaier, D.; Mohsin, M.; Chmielak, B.; Boltzen, J.; Porschatis, C.; Prinzen, A.; Matheisen, C.; Kuebart, W.; Junginger, B.; Templ, W.; Giesecke, A. L.; Kurz, H. 50 Gbit/s Photodetectors Based on Wafer-Scale Graphene for Integrated Silicon Photonic Communication Systems. *ACS Photonics* **2014**, *1*, 781–784.
- (60) Gan, X.; Shiue, R.-J.; Gao, Y.; Meric, I.; Heinz, T. F.; Shepard, K.; Hone, J.; Assefa, S.; Englund, D. Chip-Integrated Ultrafast Graphene Photodetector with High Responsivity. *Nat. Photonics* **2013**, *7*, 883–887.
- (61) Schuler, S.; Schall, D.; Neumaier, D.; Dobusch, L.; Bethge, O.; Schwarz, B.; Krall, M.; Mueller, T. Controlled Generation of a *p-n* Junction in a Waveguide Integrated Graphene Photodetector. *Nano Lett.* **2016**, *16*, 7107–7112.
- (62) Shiue, R. J.; Gao, Y.; Wang, Y.; Peng, C.; Robertson, A. D.; Efetov, D. K.; Assefa, S.; Koppens, F. H. L.; Hone, J.; Englund, D. High-Responsivity Graphene-Boron Nitride Photodetector and Autocorrelator in a Silicon Photonic Integrated Circuit. *Nano Lett.* **2015**, *15*, 7288–7293.
- (63) Purdie, D. G.; Pugno, N. M.; Taniguchi, T.; Watanabe, K.; Ferrari, A. C.; Lombardo, A. Cleaning Interfaces in Layered Materials Heterostructures. *Nat. Commun.* **2018**, *9*, 5387.
- (64) Leong, W. S.; Wang, H.; Yeo, J.; Martin-Martinez, F. J.; Zubair, A.; Shen, P.-C.; Mao, Y.; Palacios, T.; Buehler, M. J.; Hong, J.-Y.; Kong, J. Paraffin-Enabled Graphene Transfer. *Nat. Commun.* **2019**, *10*, 867.
- (65) Wei, J.; Xu, C.; Dong, B.; Qiu, C.-W.; Lee, C. Mid-Infrared Semimetal Polarization Detectors with Configurable Polarity Transition. *Nat. Photonics* **2021**, DOI: 10.1038/s41566-021-00819-6.
- (66) Sun, H.; Chen, D.; Wu, Y.; Yuan, Q.; Guo, L.; Dai, D.; Xu, Y.; Zhao, P.; Jiang, N.; Lin, C. Te. High Quality Graphene Films with a Clean Surface Prepared by an UV/Ozone Assisted Transfer Process. *J. Mater. Chem. C* **2017**, *5*, 1880–1884.
- (67) Zeng, L.; Wu, D.; Jie, J.; Ren, X.; Hu, X.; Lau, S. P.; Chai, Y.; Tsang, Y. H. Van der Waals Epitaxial Growth of Mosaic-Like 2D Platinum Ditelluride Layers for Room-Temperature Mid-Infrared Photodetection up to 10.6  $\mu\text{m}$ . *Adv. Mater.* **2020**, *32*, 2004412.
- (68) Lai, J.; Liu, Y.; Ma, J.; Zhuo, X.; Peng, Y.; Lu, W.; Liu, Z.; Chen, J.; Sun, D. Broadband Anisotropic Photoresponse of the “Hydrogen Atom” Version Type-II Weyl Semimetal Candidate TaIrTe<sub>4</sub>. *ACS Nano* **2018**, *12*, 4055–4061.
- (69) Chi, S.; Li, Z.; Xie, Y.; Zhao, Y.; Wang, Z.; Li, L.; Yu, H.; Wang, G.; Weng, H.; Zhang, H.; Wang, J. A Wide-Range Photosensitive Weyl Semimetal Single Crystal-TaAs. *Adv. Mater.* **2018**, *30*, 1801372.
- (70) Hsu, A. L.; Herring, P. K.; Gabor, N. M.; Ha, S.; Shin, Y. C.; Song, Y.; Chin, M.; Dubey, M.; Chandrakasan, A. P.; Kong, J.; Jarillo-Herrero, P.; Palacios, T. Graphene-Based Thermopile for Thermal Imaging Applications. *Nano Lett.* **2015**, *15*, 7211–7216.
- (71) Lai, J.; Liu, X.; Ma, J.; Wang, Q.; Zhang, K.; Ren, X.; Liu, Y.; Gu, Q.; Zhuo, X.; Lu, W.; Wu, Y.; Li, Y.; Feng, J.; Zhou, S.; Chen, J.-H.; Sun, D. Anisotropic Broadband Photoresponse of Layered Type-II Weyl Semimetal MoTe<sub>2</sub>. *Adv. Mater.* **2018**, *30*, 1707152.
- (72) Wang, Q.; Li, C. Z.; Ge, S.; Li, J. G.; Lu, W.; Lai, J.; Liu, X.; Ma, J.; Yu, D. P.; Liao, Z. M.; Sun, D. Ultrafast Broadband Photodetectors Based on Three-Dimensional Dirac Semimetal Cd<sub>3</sub>As<sub>2</sub>. *Nano Lett.* **2017**, *17*, 834–841.
- (73) Konstantatos, G. Current Status and Technological Prospect of Photodetectors Based on Two-Dimensional Materials. *Nat. Commun.* **2018**, *9*, 5266.
- (74) Su, P.; Han, Z.; Kita, D.; Becla, P.; Lin, H.; Deckoff-Jones, S.; Richardson, K.; Kimerling, L. C.; Hu, J.; Agarwal, A. Monolithic On-Chip Mid-IR Methane Gas Sensor with Waveguide-Integrated Detector. *Appl. Phys. Lett.* **2019**, *114*, No. 051103.